HHS Public Access

Author manuscript

Phys Med Biol. Author manuscript; available in PMC 2020 May 21.

Published in final edited form as:

Phys Med Biol. ; 64(10): 105024. doi:10.1088/1361-6560/ab155e.

Dynamic fluence field modulation in computed tomography using multiple aperture devices

Grace J Gang[1], **Andrew Mao**[1], **Wenying Wang**[1], **Jeffrey H Siewerdsen**[1], **Aswin Mathews**[1], **Satomi Kawamoto**[2], **Reuven Levinson**[3], **J Webster Stayman**[1,4]

[1]Department of Biomedical Engineering, Johns Hopkins University, Baltimore, MD, United States of America

[2]Department of Radiology and Radiological Science, Johns Hopkins University, Baltimore, MD, United States of America

[3]Philips Healthcare, Haifa, Israel

Abstract

A novel beam filter consisting of multiple aperture devices (MADs) has been developed for dynamic fluence field modulation (FFM) in CT. Each MAD achieves spatial modulation of x-ray through fine-scale, highly attenuating tungsten bars of varying widths and spacings. Moiré patterns produced by relative motions between two MADs provide versatile classes of modulation profiles. The dual-MAD filter can be designed to achieve specific classes of target profiles. The designed filter was manufactured through a laser-sintering process and integrated to an experimental imaging system that enables linear actuation of the MADs. Dynamic FFM was achieved through a combination of beam shape modulation (by relative MAD motion) and amplitude modulation (by view-dependent mAs). To correct for gains associated with the MADs, we developed an algorithm to account for possible focal spot changes during/between scans and spectral effects introduced by the MADs. We performed FFM designs for phantoms following two imaging objectives: (1) to achieve minimum mean variance in filtered backprojection (FBP) reconstruction, and (2) to flatten the fluence behind the phantom. Comparisons with conventional FFM strategies involving a static bowtie and pulse width modulation were performed. The dual-MAD filter produced modulation profiles closely matched with the design target, providing varying beam widths not achievable by the static bowtie. The entire range of modulation profiles was achieved by 0.373 mm of MAD displacement. The correction algorithm effectively alleviated ring artifacts as a result of MADs while preserving phantom details such as wires and tissue boundaries. Dynamic FFM enabled by the MADs were effective in achieving the imaging objectives and demonstrated superior FFM capabilities compared to the static bowtie. In an ellipse phantom, the FFM of objective 1 achieved the lowest mean variance in all cases investigated. The FFM of objective 2 produce nearly isotropic local noise power spectrum and homogeneous noise magnitude. The dual-MAD filter provides an effective tool for fluence control in CT to overcome limitations of conventional static bowties and to further enable patient-specific FFM studies for a wide range of dose and image quality objectives.

[4]Author to whom any correspondence should be addressed. web.stayman@jhu.edu.

Keywords

dynamic bowtie; adaptive imaging; CT image quality; x-ray filtration; task-driven imaging; optimized data acquisition

1. Introduction

Fluence modulation is routinely practiced in computed tomography (CT) to reduce radiation dose and lower dynamic range requirements of the detector (Toth (2002) and Kalra *et al* (2004)). Current CT systems offer fluence control through a combination of tube current modulation (TCM) and static bowtie filters. The former allows the adjustment of overall fluence level across projection angles (θ) while the latter applies a static beam-shaping filter along the transverse detector direction (u) that approximately complements the attenuation through, for example, different-sized cylinders simulating different anatomcal sites such as body and head. While such fluence modulation improves dose utilization as compared to an unmodulated x-ray beam, the modulation profile is limited due to the static nature of the bowtie. Due to heterogeneity within the patient, oblateness of the patient cross-section, and variations of patient size and anatomy in the longitudinal direction (e.g. from shoulder to abdomen), attenuation characteristics can vary strongly across detector elements and projection angles. Since technique protocols generally need to ensure sufficient signal-to-noise (SNR) in the most attenuated rays, using a single fluence modulation profile for all projection angles significantly limits dose reduction capability. Furthermore, a static bowtie cannot account for patient mis-centering - a frequent occurrence in 46% of patients in a study by Toth *et al* (2007), where the bowtie itself may even impart surface dose penalties up to 140%.

To address these limitations, dynamic FFM has been proposed in which the x-ray beam shape can be modulated along the transverse detector direction and allowed to change as a function of projection angles (Graham *et al* 2007). Various theoretical dynamic FFM profiles have been proposed to demonstrate improved dose utilization using a variety of image quality objectives. For general CT applications, a common FFM objective involves homogenizing fluence behind the patient to ensure sufficient signal-to-noise ratio (SNR) in all rays, to lower dynamic range requirements of the detector, and to reduce unnecessarily high radiation dose to the edge of the patient. Dynamic FFM has also been proposed to minimize the mean variance in filtered-backprojection (FBP) reconstruction by varying the barebeam fluence as a function of the square root of the line integral (Harpen 1999). Other objectives include achieving a user-prescribed, spatially-varying SNR map while considering dose constraints (Bartolac *et al* 2011), minimizing the peak variance or a weighted mean variance in FBP reconstruction (Hsieh and Pelc 2014) and maximizing global imaging performance of a detection task in model-based reconstruction through a patient-specific and task-specific FFM (Gang *et al* 2017). Dynamic FFM also enables volume-of-interest (VOI) imaging capability in which only a predefined VOI is fully illuminated in each view while the rest of the patient receives much lower dose (Heuscher and Noo 2011, Szczykutowicz and Mistretta 2014, Wang *et al* 2018).

Despite these advantages, hardware development to realize dynamic FFM has many challenges and remains an ongoing research effort. To be compatible with current diagnostic CT systems, FFM hardware needs to keep up with high gantry rotation speeds and must exhibit a small form factor to fit within the limited collimator space in a CT gantry. Many FFM hardware designs have been proposed to date, typically achieving fluence modulation across the field via attenuation through variable material thickness. Simple designs consist of dynamic filters in which a small number (2–3) of moving components are used to provide a limited class of modulation patterns (Toth *et al* 2006 and Liu *et al* 2014). Recent efforts have focused on providing more flexible classes of modulation profiles to better accommodate patient-specific imaging needs. A piecewise-linear dynamic bowtie has been proposed that employs multiple triangular wedges (in the transverse direction) with varying thickness along the longitudinal direction (Hsieh and Pelc 2013 and Hsieh *et al* 2014). Dynamic FFM was achieved by independently translating each wedge throughout the scan to deliver flexible, piece-wise linear modulation profiles. Other examples include a digital beam attenuator using dynamically translated triangular prisms to achieve piece-wise constant modulation profiles (Szczykutowicz and Mistretta 2013a, 2013b, Szczykutowicz and Mistretta 2014) and fluid-filled dynamic filter designs that consist of a 2D array of cells/channels that changes local attenuation through varying fluid levels (Szczykutowicz and Hermus 2015, Shunhavanich *et al* 2015, Hermus and Szczykutowicz 2016).

This work reports the development of a novel dynamic beam filter based on multiple aperture devices (MADs). A MAD consists of fine-scale, highly-attenuating bars and through-hole apertures that act as fine-scale binary filters and provide nearly continuous spatial modulation along the transverse direction of the detector. Shifting two such devices relative to each other produces Moiré patterns that effect a wide range of fluence modulation profiles. The proposed dual-MAD filter offers several major advantages: (1) a compact form factor that can be retrofitted into existing CT gantries; (2) a wide range of fluence modulation profiles that can be generated using a small (sub-mm) range of motion, which reduces the burden on the mechanical system under fast rotation of the CT gantry; and (3) flexible and smoothly varying modulation profiles for patient-specific and task-specific image quality and dose objectives. Initial proof-of-concept of the dual-MAD filter has been presented in previous work (Mathews *et al* 2016, Stayman *et al* 2016 and Mathews *et al* 2017). This manuscript reports implementation of the dual-MAD filter on an experimental imaging bench and evaluation of MAD-enabled FFM on different phantoms to achieve image quality objectives.

2. Methods

2.1. Operation principles

We propose the dual-MAD filter as an alternative to the current paradigm of static bowties as a pre-patient beam filter. Figure 1(a) shows the dual-MAD filter placement within a CT scanner and illustrates coordinate notations. Traditional bowtie designs typically achieve spatial fluence modulation via varying material thickness. In contrast, the MAD relies on fine-scale, variable-width bars and through-hole apertures to control the amount of local x-ray attenuation (Stayman *et al* 2016). Figure 1(b) illustrates x-ray transmission through a

single MAD (designated as MAD0) for a parallel x-ray beam. The bars (red) block the x-rays using a high atomic number attenuator such as tungsten whereas the apertures allow x-rays through without any attenuation. Similar illustrations can be made for a fan-beam or cone-beam geometry in which the MAD bars are back-focused towards the source. The MAD exhibits periodic structure in which the transmission within each period is the ratio between the aperture size (equal to pitch minus bar-width) and the pitch. By varying bar-widths and aperture sizes within different periods, different fractions of the x-ray beam are transmitted, thus achieving an arbitrary spatial fluence modulation profile or beam shape.

While a single MAD ahieves only a static profile, additional fluence modulation profiles can be produced by placing two MADs in series as shown in figure 1(c). X-rays blocked by either MAD decreases local fluence. Relative motion between the two MADs therefore changes the amount of local attenuation. In particular, the two MADs produce Moiré interference patterns that vary as a function of the relative displacement, Δ. Figure 1(c) illustrates an example where the fluence profile narrows as MAD1 is shifted relative to MAD0. Within each period, the dual-MAD filter can achieve approximately continuous (up to the precision of Δ) fractional transmission ranging from completely overlapping bars (minimum blockage, maximum transmission) to completely non-overlapping bars (maximum blockage, minimum transmission). Continuous spatial modulation across detector elements is also possible through appropriate design of bar-widths and aperture sizes. Beam shape modulation enabled by view-dependent Δ can be coupled with beam intensity modulation enabled by TCM to achieve dynamic FFM.

2.2. Design

The dual-MAD design offers flexibility in the class of achievable fluence modulation profiles. The design process has been reported in Mathews *et al* (2016) and will be briefly summarized in this section. The MAD design can be formulated as an optimization problem in which we identify the spatial arrangements of bars and apertures to yield the closest match to a set of target fluence profiles under various manufacturing constraints. For MADs reported in this work, the target fluence profiles were specified to flatten the detected signal behind the anterior-posterior (AP) and lateral views of a uniform acrylic phantom of the same shape and dimension (30 × 20 cm) as that of the QRM liver phantom (QRM GmbH, Germany). We sought low dimensional parameterizations of the bar widths and apertures using sinusoidal basis functions, and optimized the coefficients using a covariance matrix adaptation evolution strategy (CMA-ES) algorithm (Hansen and Ostermeier 1996).

The MADs reported in this work were designed for an experimental cone-beam CT (CBCT) benchtop system, illustrated in figure 2(a). Geometry parameters of the system are summarized in table 1. The source-to-MAD distance, SMD, is measured from the source to the mid-plane between two MADs and determines the physical size of the dual-MAD filter. The dimension of each MAD is 14.5 cm along u in the detector domain and 1.5 cm along v, offering 34.0 × 3.5 cm coverage at isocenter. Each MAD was manufactured from 2 mm of tungsten through a powder bed laser sintering process (Smit-Rontgen Facility, Best, Netherlands). The spacing between the two MADs was 10 mm for a compact design.

2.3. Implementation and assessment on an experimental imaging bench

2.3.1. Imaging bench—The dual-MAD filter was installed on the experimental imaging bench as illustrated in figure 2(a). Each MAD was attached to a linear actuator (Velmex Inc., Bloomfield, NY) with translation encoding precision of 2 μm. The vertical centers of the MADs were aligned with the central v-axis of the flat-panel detector to emulate the degree of beam divergence on a diagnostic CT scanner. The actuators can be controlled synchronously with the motion stage and a step-and-shoot x-ray exposure.

The benchtop system employs an x-ray generator (CPI, Georgetown, ON, Canada) that has been customized to deliver view-dependent pulse width ranging from 0.1 to 60 ms, thereby enabling exposure modulation through pulse width control at a fixed tube current (ordinarily achieved through TCM in a diagnostic CT scanner).

2.3.2. Imaging phantoms and phantom-specific FFM design—Three phantoms (figure 2(b)) were used for experimental evaluation of dynamic FFM using MADs: (1) an elliptical PMMA phantom (major axis = 25.8 cm, minor axis = 14.1 cm); (2) a CatPhan module (CTP404, Phantom Laboratory, Greenwich, NY) with four slanted wires and various cylindrical contrast inserts; and (3) an anthropomorphic head phantom (Atom, CIRS, Norfolk, Virginia, USA). For each phantom, we designed phantom-specific FFM following three imaging objectives:

1. *Unmodulated*: the phantoms were imaged without MADs at a constant pulse width.
2. *Flat-field*: spatial modulation is applied such that the fluence behind the object reaching the detector is uniform across detector locations (u) and across projection angles (θ). Mathematically, assuming the line integral (l) of the phantom is known, the barebeam fluence field to be delivered is given by the following equation when α = 1.0:

$$I_0(u^*,\theta) = \frac{\exp[\alpha l(u^*,\theta)]}{\sum_\theta \exp[\alpha l(u^*,\theta)]} I_0^{tot}. \quad (1)$$

Here, I_0 denotes the target barebeam fluence, l denotes the line integrals of the object, and u^* denotes detector elements behind the phantom such that only fluence going through the object counts toward the total fluence budget, I_0^{tot}. To find the fluence pattern in practice, estimates of l are required. There are various ways to obtain l prior to scanning. Previous work proposed a low-dose 3D scout acquired at approximately the same total exposure as conventional AP and lateral scouts, allowing computation of l using a forward projector according to the geometry of the imaging system (Yin *et al* 2015, Gomes *et al* 2017). Alternatively, the object can be approximated as a rectellipse based on intensity values in the AP and lateral scouts (Mao *et al* 2018). In this work, we approximated each phantom as an ellipse based on physical measurements of its major and minor axes.

3. *Minimum mean variance in FBP*: Harpen (1999) proved that the mean variance over the object in an FBP reconstruction is minimized when the barebeam fluence field follows equation (1) with $\alpha = 0.5$.

Displacements of MAD1 as a function of projection angles, Δ_θ, and pulse width modulation, $t(\theta)$, were identified for the target FFM required for objectives (2) and (3) for each phantom. To obtain Δ_θ, the target profiles were first compared with a MAD calibration scan. Due to the periodic nature of MADs and smoothly varying barwidths, the range of fluence profiles achieved as Δ is incremented over adjacent periods is very similar, i.e. MAD response is nearly periodic as a function of Δ (over several periods). Dynamic FFM can therefore be achieved using profiles within a single period to minimize the range of MAD displacement. Furthermore, some profiles within the period are bimodal or overly narrow, and can therefore be excluded for design purposes. Therefore, the MAD calibration scan was performed over Δ values through a 0.328 mm range with 0.002 mm increments. The periodic MAD response and the profiles used for the design are illustrated in the Results section in figure 3(a). The optimal Δ was identified by minimizing the root mean square error between maximum-normalized target and calibration. To obtain $t(\theta)$, the pulse width for each view was calculated as t_0 (the pulse width used in calibration) times the scale factor required by the central detector element in the calibration scan to achieve the signal level required in the target profile.

2.3.3. Corrections—The presence of MADs introduces an additional gain term (g_M) in the data forward model:

$$y(u, v, \theta) = t(\theta) g_M(u, v; \Delta_\theta) g_{B_0}(u, v) g_D(u, v) e^{-l(u, v, \theta)} \quad (2)$$

where y and l respectively denote the projection measurements and line integrals, both spanning the detector domain, (u, v), and projection angles, θ. Typical gain factors associated with the inherent x-ray beam shape and detector sensitivity are denoted as g_{B_0} and g_D, respectively. View-dependent pulse width modulation is denoted as $t(\theta)$. The parameter g_{B_0} represents the beam unfiltered by the MADs at unit pulse width (1 ms) and at the nominal fixed tube current used in the study. The g_M term is a function of view-dependent MAD1 displacements, Δ_θ. Ideally, all MAD gain effects can be modeled with a single gain calibration scan with the MADs in air at the same Δ_θ as the object scan. We term this method ‘simple correction’.

Early observations indicate that the simple correction method cannot completely model physical effects from the MAD bar structures in the projection data. Consequently, high frequency ring artifacts can appear in axial slices of the reconstruction. We postulate that this is due to two physical effects: (1) focal spot shift/blooming during the scan and between scans causing mismatches between g_M in the data and the calibration scans; (2) beam hardening/spectral effects from oblique x-rays grazing the edge of the tungsten bars. These effects can be described in a modified forward model as:

$$y(u,v,\theta) = t(\theta) g_M(u,v;\Delta_\theta) g_B(u,v) g_D(u,v) e^{-\kappa(u,v;\Delta_\theta) l(u,v,\theta)} \quad (3)$$

where κ carries the same dependencies as g_M and accounts for spectral effects from the MADs, similar to a 1st order beam hardening correction factor (Joseph and Spital 1978). In relation to equation (1), the I_0^{tot} term is equal to $t(\theta) g_B(u,v) g_M(u,v;\Delta_\theta)$.

We propose a 'full model correction' method to cancel out $t(\theta)$, g_M, and κ to recover l from equation (3). Since $t(\theta)$ and Δ_θ depend on the object and the imaging objective, we devised the correction method such that only one set of calibration scans needs to be acquired for all combinations of $t(\theta)$ and Δ_θ. Brief descriptions of the correction steps and the associated calibration scans are summarized below. Mathematical details of each step are provided in appendix.

1. g_{B_0}, g_D, and t calibration using air gain scans (denoted as A): gain scans in air were acquired at a range of pulse widths to calibrate for g_{B_0}, g_D, and the delivered $t(\theta)$.
2. g_M calibration using MAD gain scans (denoted as M): a focal spot monitoring method and blur correction operation was used to match g_M in the data and the calibration scans.
3. κ calibration using PMMA gain scans (denoted as P): scans of PMMA blocks of different thicknesses were used to calibrate κ using a 1st order beam hardening correction.

Following all correction steps, the line integrals can be recovered from equation (3) and used for reconstruction.

2.3.4. Reconstructions—Filtered backprojection (FBP) was performed using estimated line integrals following previously described data correction methods (sections 2.3.3) for comparison. All reconstructions were performed at an isotropic voxel size of 0.5 mm. The FBP reconstructions used a Hann filter and a cutoff frequency of 0.8 mm^{-1}.

2.4. Image quality assessment

To assess the effectiveness of the MAD correction algorithms, projection data and reconstructed images were visually assessed for the presence of residual bar patterns and ring artifacts. Due to the cylindrical shape of the CatPhan module, FFM designed for such phantoms has a fixed relative displacement between the MADs (i.e. no MAD motion during scan) and constant pulse width for all projections. The CatPhan module was therefore imaged with FFM designed for the ellipse to assess image quality implications of the correction algorithm on a more challenging scenario in terms of the range of Δ values and pulse width variations.

To assess the effectiveness of the dual-MAD filter in achieving dynamic FFM objectives, the local noise power spectrum (NPS) was analyzed for the ellipse phantom at seven locations

for the unmodulated acquisition, the a = 0.5 (Minimum variance for FBP), and a = 1.0 (Flat-field) strategies outlined in section 2.3.2. We acquired two repeated scans for each imaging objective, performed the full-model correction, and took the difference between the reconstructions. The 2D NPS was computed from the sample average over a total of 17 axial slices according to:

$$\mathrm{NPS} = \frac{a_x a_y}{2N_x N_y}\left\langle \left| \mathcal{FT}\left\{\mu_1 - \mu_2\right\}\right|^2 \right\rangle \tag{4}$$

where a_x and a_y are voxel sizes along x and y, N is the size of the ROI (49 × 49 voxels), μ_1 and μ_2 indicate reconstructions from two repeated scans, and $|\cdot|$ and $\langle\cdot\rangle$ indicate absolute value and sample average, respectively. In addition, noise uniformity was examined through variance maps calculated by marching a 3 × 3 ROI along each voxel location through an axial slice of the reconstruction. The noise characteristics were compared with theoretical expectations.

2.5. Comparison with a static bowtie

To compare the dual-MAD filter with conventional FFM strategies on CT scanners, we performed similar phantom-specific designs (section 2.3.2) and image quality analysis (section 2.4) for the elliptical phantom using a static bowtie filter with pulse width modulation. The bowtie filter was made of aluminum and designed to provide flat signal levels behind a 32 cm body CTDI phantom. Data correction for the static bowtie acquisition corresponds to the ‘simple correction’ scheme in section 2.3.3 where gain scans with the bowtie in air is divided from the data. The comparison focuses on capabilities of the two strategies to achieve specific FFM objectives.

3. Results

3.1. Phantom-specific FFM design

The MAD profiles (gain, offset-corrected) measured from the CBCT bench as a function of MAD1 displacements, Δ, are shown in figure 3(a). The MAD response exhibits periodic behavior as a function of Δ and is almost symmetric within each period. For phantom-specific FFM designs, we used profiles within a single period corresponding to Δ values from 0.4 to 0.7 mm as indicated on figure 3(a). The FFM designs for the ellipse phantom following the a = 0.5 and a = 1.0 imaging objectives are shown on figure 3(b). Both the target (left) and achieved (right) profiles are shown as the ratio to the fluence level in an unmodulated acquisition under the same total fluence constraint (I_0^{tot}). The achieved profiles are slightly wider than the theoretical target to ensure non-zero transmissivity (5%) at the edge. Pulse width modulation scales the fluence profile such that the magnitude is well matched between target and achieved. The root mean square error between the target and achieved profiles behind the object is 0.172 and 0.298 for the a = 0.5 and a = 1.0 cases, respectively.

Similar plots are shown for the bowtie filter. Figure 3(c) presents the single achievable bowtie modulation profile without pulse width modulation as a function of projection

angles. Figure 3(d) shows capabilities of the bowtie in achieving the $\alpha = 0.5$ and $\alpha = 1.0$ target profile. Compared with figure 3(b), the bowtie is not able to accommodate the changing beam width. The mismatch is especially severe for narrower profiles around 90° and 270°. The root mean square error for the bowtie acquisitions is 0.347 and 0.703 for the $\alpha = 0.5$ and $\alpha = 1.0$ cases, respectively, indicating worse agreement between the target and achieved profiles compared to the dual-MAD acquisitions.

3.2. Corrections for MADs

Figure 4 illustrates the projections of the elliptical phantom under the $\alpha = 0.5$ FFM strategy following corrections schemes detailed in section 2.3.3: a simple correction in which we assume no focal spot changes or spectral effects and hence consistent g_M between y and M, and a full model correction with both blur and spectral corrections using all calibration scans. We further included an intermediate step following blur correction (termed 'blur only') to match the g_M in y and M but ignoring spectral effects. We present the corrected sinogram and zoom in on three regions of interest (ROIs). Each ROI contains 10 projections with 10 detector rows in each, to illustrate the extent of high frequency bar patterns due to the MADs along the v direction. In all three ROIs, residual MAD bar patterns are visible in the simple correction scheme, reduced in the blur only correction, and least visible in the full model correction scheme. Furthermore, the bars are more obvious in the middle (ROI 1) and right half (ROI 3) of the projections, where blur correction alone is insufficient to remove the bars.

The reconstructions of the elliptical phantom using each of the three correction schemes are shown in figure 5. Residual bar patterns in the projections result in high frequency ring artifacts in axial slices and bands in the coronal and sagittal slices of the reconstruction. Consistent with observations in figure 4, the artifacts are the most conspicuous for the simple correction scheme, reduced in the blur only correction, and least visible in the full model correction. Slight ring artifacts are still present at edges of the ellipse along the major axis, likely due to low fluence levels in these regions. While ring artifacts due to the MADs have been greatly reduced, we note in all three reconstructions comparable levels of shading artifacts, typical of cone-beam CT acquisitions.

Reconstructions of the two non-uniform phantoms are shown in figure 6 for the CatPhan sensitometry module and the Atom head phantom. An axial slice through the reconstruction and zoomed ROIs are shown for the full model and simple correction for comparison. The full model correction is effective in removing ring artifacts for non-uniform phantoms. Moreover, phantom details such as wires, small and large contrast inserts, and bone boundaries are preserved. There is no visible loss of resolution as a result of the full model correction methods.

3.3. Image quality assessment

The noise characteristics of the ellipse phantom following the three FFM strategies detailed in section 2.3.2 are presented in figure 7. Analysis for the dual-MAD filter were performed for reconstructions using the full model correction method. The reconstructed slice and difference image between two repeated scans show strongly correlated noise along the long-

axis of the ellipse for an unmodulated acquisition. The streaks are visibly reduced in the α = 0.5 and α = 1.0 strategies. Note that a small bias is present between the unmodulated and the two MAD reconstructions, likely due to beam hardening effects as a result of the MADs.

Local NPS are shown at seven locations within the ellipse phantom to further illustrate noise structure and magnitude. The α = 0 strategy exhibits typical location-dependent and anisotropic NPS as a result of varying path lengths through each location as a function of rotation angles (Gang *et al* 2014). The noise magnitude decreases from the center to the edge as expected. The α = 0.5 strategy using both dual-MAD and bowtie presents similar anisotropy but the variation in magnitude is smaller. The NPS from the α = 1.0 strategy using the dual-MAD filter is almost isotropic with more homogeneous magnitude. The lower noise region along f_y is due to overexposure along x (compared to the ideal α = 1.0 FFM), which is consistent with the wider achieved fluence profiles around 90° and 270° in figure 3(b). In comparison, the NPS from the bowtie α = 1.0 strategy is less isotropic and still exhibits strong directionality, especially for locations away from the central axis of the ellipse. In term of noise magnitude, the variance map of the dual-MAD α = 1.0 strategy is much flatter compared to all other cases. The dual-MAD α = 0.5 case has the lowest mean variance among all five acquisitions. These observations indicate that the dual-MAD filter was able to achieve image quality objectives consistent with theoretical expectations, while convetional FFM strategies with a static bowtie was not as effective.

4. Discussion

This work presents the implementation and assessment of a novel dynamic filter using dual multiple aperture devices. Each MAD was affixed to a linear actuator and installed on an experimental benchtop system. Dynamic FFM was achieved with view-dependent MAD displacement coupled with pulse width modulation at a constant tube current. A correction algorithm was developed to account for focal spot changes within/between scans and spectral effects resulting from the MADs to produce nearly artifact-free reconstructions. Three imaging objectives were investigated for FFM designs: unmodulated, minimum mean variance in FBP (α = 0.5 in equation (1)), and flat field behind the phantom (α = 1.0 in equation (1)). The FFM delivered by the dual-MAD filter closely approximates the theoretical target profiles and shows better agreement compared to conventional FFM strategy with a static bowtie filter. The resulting noise characteristics in an ellipse phantom matched theoretical expectations, with the minimum mean variance objective yielding the lowest mean variance among all cases investigated, and the α = 1.0 objective presenting nearly homogeneous noise magnitude and isotropic NPS.

The dual-MAD filter has several advantages compared to static bowties and other dynamic filter designs introduced in section 1. For ellipsoidal objects considered in this work, a wide range of beam width can be achieved with just 0.373 mm of linear translation of MAD1. The single degree of freedom faciliates calibration and quality assurance; the small range of motion reduces the velocity and acceleration requirements of the actuation system under the high rotation speed of the CT gantry. In addition, the manufactured dual-MAD filter (without actuators) has a small form factor at approximately 15 × 2.8 × 1.4 cm, which can

easily fit into the limited collimator space in existing CT gantries. Implementation and assessment of the dual-MAD filter on a CT gantry is currently underway.

Results from this work demonstrated capability of the dual-MAD filter in enabling dynamic FFM for different phantoms and imaging objectives. As shown in figure 3, the dual-MAD filter can produce a wide range of fluence modulation profiles to better accommodate different patient cross-sections compared to a static bowtie. By using different designs of bars and apertures, the dual-MAD can also provide flexibility in the classes of achievable modulation profiles to enable customizable and anatomy-specific FFM designs, e.g. bimodal profiles for the thorax.

For the class of modulation profiles presented in this work, the dual-MAD filter decreases the transmissivity to around 50% at the maximum (center of the beam). The reduction in maximum transmissivity requires greater tube loading to deliver the same fluence compared to conventional bowtie filters. We have since improved the MAD design process to increase the maximum transmissivity to 85%, which is only limited by the minimum bar-width (150 μm) based on manufacturing constraints. The new MADs are the subject of ongoing work. To further reduce tube loading, one might remove the central bars to increase maximum transmissivity to 100%; however, the ability to modulate the center of the beam would be compromised. The minimum transmission at the edge of the field can also be important for identifying barebeam fluence levels for reconstruction purposes. The design process in this work does not include constraints/penalty for a minimum transmission level at the edge of the field. Imposing such constraints, however, reduces the flexibility in achieving certain beam shapes, especially for smaller objects which requires narrower beam widths. Both the maximum and minimum transmission can be increased by using a lower atomic number material for the bars (with potentially more complex beam hardening effects). Such design considerations will be the subject of future work.

Accurate gain corrections are especially important for CT systems with dynamic beam filters to produce artifact-free reconstructions. The benchtop system in this work poses significant challenges for gain corrections due to focal spot changes within and between scans. We developed a full model correction method to demonstrate the capability to achieve mostly ring-artifact-free reconstruction in the presence of dynamic dual-MAD filter. For initial implementation, we reserved the top half to one-third of the filter in air for focal spot monitoring (see appendix). Future developments will use a fiducial at the edge of the field to achieve such purpose and geometrically scale the blur function to the rest of the field. Other focal spot monitoring tools may provide more accurate states of the focal spot and could also be used for blur corrections. More importantly, the focal spot on x-ray tubes in diagnostic CT scanners is likely to be more stable than the fluroscopy x-ray tube used in these experimental studies, which may allow the blur correction step to be circumvented altogether. Future work would examine the above methods for accurate gain corrections while imaging through the full longitudinal field of view of the dual-MAD filter.

The studies presented in this work focused on centered patients, i.e. the beam shape changes throughout the scan but the beam center is stationary. We achieved this by moving only MAD1 relative to MAD0. For miscentered patient and VOI imaging, both MADs can be

moved simultaneously to change both the beam center and beam shape. In this case, the calibration scans needs to include displacements (Δ values) of both MADs. The same correction algorithm can be applied in this case and have been shown to yield mostly artifact-free reconstructions (Mao *et al* 2018).

For clinical implementation of the dual-MAD filter, we identify the following areas for future investigations. First, implementation of the dual-MAD filter on a diagnostic CT gantry is currently underway with an actuation system capable of translations of 3000 mm s^{-1} with up to 6 μm precision. Assessment of FFM for different phantoms and imaging objectives on the CT gantry will be presented in future work. Second, the correction method was designed such that only one set of calibration scans (including air, MAD, PMMA gain scans) need to be acquired for arbitrary FFM. How long the calibration files will remain viable depends on the stability and reproducibility of the x-ray source, the detector, and the actuation system. The frequency of MAD calibration will be determined for the particular CT system. Third, FFM capabilities provided by the dual-MAD filters enables the investigation of additional image quality and dose objectives in real data. Previous work from our group has demonstrated the dual-MAD filter as an efffective tool to achieve VOI imaging (Wang *et al* 2018) and to accommodate miscentered patients and avoid dose penalties (Mao *et al* 2018). Experiments are currently underway to evaluate task-driven FFM designs for model-based iterative reconstruction.

5. Conclusion

We have reported the development of a dual-MAD filter for dynamic beam shaping in CT and CBCT. This work paves the way for the implementation and evaluation of dynamic FFM on a diagnostic CT gantry to overcome limitations of conventional static bowties. The dual-MAD filter can be used to provide flexible FFM profiles that accommodate changing body cross-sections across rotation angles and shifting beam centers for miscentered patients to avoid image quality and dose penalties. Furthermore, the dual-MAD filter enables the investigation of patient-specific FFM studies for a wide range of dose and image quality objectives including task-driven FFM and VOI imaging for improved image quality and/or reduced radiation dose.

Acknowledgment

This work is supported by NIH grant U01EB018758. Part of this research project was conducted using computational resources at the Maryland Advanced Research Computing Center (MARCC).

Appendix.: Full model correction of MAD gains

As described in section 2.3.3, to account for focal spot changes and spectral effects from the MAD, we introduced the following modified data forward model:

$$y(u,v,\theta) = t(\theta) g_M\left(u,v;\Delta_\theta\right) g_B(u,v) g_D(u,v) e^{-\kappa\left(u,v;\Delta_\theta\right) l(u,v,\theta)}. \tag{A.1}$$

To recover l, we proposed a ‘full model correction’ method with the following correction steps and calibration scans:

1. g_{B_0}, g_D, and t calibration using air gain scans (denoted as A): While the combined effect of g_{B_0} and g_D are fairly straightforward to calibrate, the $t(\theta)$ delivered during the dynamically modulated scan may be different from that commanded due to rise/fall times of the generator. To account for this effect, we adopted a multi-point gain correction method where thirty repeat air scans (without MADs) were taken at a range of pulse widths from 2.21 ms (lowest pulse width available) to 37 ms (detector signal just below saturation). The air scans were offset-corrected and averaged at each pulse width. We performed a linear fit on the mean signal within a small air region as a function of pulse width and used the mean signal with the same region in each view of the data y to obtain the actual $t(\theta)$ delivered. In addition, we computed a pixel-by-pixel response from the averaged air gains as a function of t, $A(u, v) = a(u, v)t + b(u, v)$. Substituting in the delivered $t(\theta)$, we obtain:

$$A(u, v, \theta) = a(u, v)t(\theta) + b(u, v) = t(\theta)g_{B_0}(u, v)g_D(u, v)\,. \tag{A.2}$$

Dividing y by A therefore cancels out $g_{B_0}(u, v)$, $g_D(u, v)$, and $t(\theta)$.

2. g_M calibration using MAD gain scans (denoted as M): MAD gain scans were acquired at the same set of Δ values used for FFM design (section 2.3.2). Five repeats were acquired at each Δ position and averaged. We then assemble M according to the commanded Δ_θ. The scan was acquired at a nominal pulse width, t_0 = 10 ms, with no object in the beam. The MAD gain scan is mathematically expressed as:

$$M\left(u, v; \Delta_\theta\right) = t_0 g_M^*\left(u, v; \Delta_\theta\right) g_B(u, v) g_D(u, v) \tag{A.3}$$

where superscript * indicates potential mismatch in g_M from that in y due to focal spot changes. The air gain for t_0 (denoted as A_{t_0}) can be obtained from the multi-point calibration in the previous section and divided from M to obtain g_M^*.

To match g_M^* to g_M, a method for focal spot monitoring is required. In this work, the object was positioned to only occupy the bottom half to two thirds of the dual-MAD field of view. The remaining 'air' data were used for a view-by-view estimation of focal spot changes between the reference image $y/A = g_M(u, v; \Delta_\theta)$ and the moving image $M/A_{t_0} = g_M^*\left(u, v; \Delta_\theta\right)$. Both sets of data were first averaged along the v direction over 18 detector rows to reduce noise. To accommodate spatially variant blur, for each projection angle θ, the resulting 1D profiles along u were divided into local segments of 99 pixels with a 5 pixel overlap to ensure smooth transitions between neighboring segments. Each segment was normalized by a Gaussian-smoothed version of itself (i.e. a local mean normalization) to eliminate potential mismatch between the mean of the reference and moving segments (e.g. due to scatter from the object). A 1D blur kernel was then fitted to

each normalized segment so as to minimize the sum of squared error between g_M and the blurred g_M^*, i.e.

$$\underset{b(u)}{\operatorname{argmin}} \sum_{u_s} \left[\breve{g}_M(u_s, \Delta_\theta) - b_s(u) \otimes \breve{g}_M^*(u_s, \Delta_\theta)\right]^2 \tag{A.4}$$

where ˘ indicates the local mean normalization described above, u_s is the extent of the local segment, and $b_s(u)$ is an 11-element area-normalized blur kernel for that segment. In this work, $b_s(u)$ was optimized using the BFGS algorithm with an initialization equal to a centered impulse for the first segment in each projection, and to the optimization result from the previous segment for subsequent segments. To apply the local blur kernels to M, we simply need to reverse the above process for each row of M (instead of averaging over rows). Using subscript b to denote blur-corrected data, $M_b/A \approx g_M(u, v; \Delta_\theta)$ and can therefore be divided from y/A.

3. κ calibration using PMMA gain scans (denoted as P): the spectral effect, κ, can be calibrated using a 1st order beam hardening correction. We scanned rectangular PMMA blocks of constant thickness along u and v at four total thicknesses: 2, 4, 6, and 8 inches. The scans were performed at the same nominal t_0 through the same range of Δ values as that of the MAD gain scan. For each thickness (denoted as j), the PMMA scan can be represented as:

$$P^j = t_0 g_M^* * (u, v; \Delta_\theta) g_B(u, v) g_D(u, v) e^{-\kappa(u, v; \Delta_\theta) l_{pj}(u, v)} \tag{A.5}$$

where l_{Pj} denotes the line integral of the PMMA block of thickness j.

We first performed blur correction for each P^j according to methods in the previous section to match $g_M^* *$ with g_M. Then, ideally, $\kappa(u, v; \Delta_\theta)$ can be calculated as the slope of $-\log\left(P_b^j / M_b\right)$ as a function of $l_{Pj}(u, v)$. However, $l_{Pj}(u, v)$ is generally unknown. In addition, due to focal spot changes between scans, the κ calculated from the PMMA scans may be slightly mismatched from that in the data. We therefore substitute $l_{Pj}(u, v)$ with the physical thickness of the PMMA blocks and find the appropriate scaling/normalization of the slope at each pixel based on the following empirical criteria: (1) the mean of κ should be 1 to preserve the magnitude of the line integrals; and (2) a proper scaling of the slope should minimize MAD bar patterns in the data. Defining $\kappa^*(u, v, \Delta_\theta)$ to be the slope of $-\log\left(P_b^j / M_b\right)$ as a function of thickness j, κ is then equal to $a_\kappa \kappa^* + 1 - \overline{a_\kappa \kappa^*}$, where a_κ is a scalar that captures the proper scaling. We optimized for a_κ according to the following flatness criterion:

$$\underset{a_\kappa}{\operatorname{argmin}} \sum_u \left\{ \frac{\left\langle -\log\left(\frac{y/A}{M_b/A}\right)\right\rangle_v}{a_\kappa\langle\kappa^*\rangle_v + 1 - \overline{a_\kappa\langle\kappa^*\rangle_v}} - \mathcal{G} \otimes \left[\frac{\left\langle -\log\left(\frac{y/A}{M_b/A}\right)\right\rangle_v}{a_\kappa\langle\kappa^*\rangle_v + 1 - \overline{a_\kappa\langle\kappa^*\rangle_v}} \right] \right\}^2 \tag{A.6}$$

where $\frac{-log\left(\frac{y/A}{M_b/A}\right)}{a_\kappa\langle\kappa^*\rangle_v + 1 - \overline{a_\kappa\langle\kappa^*\rangle_v}}$ is the corrected line integrals (l in equation (3)) of the phantom, averaged over 70 detector rows indicated by $\langle\rangle_v$ to reduce noise; $\mathcal{G}$ is a Gaussian kernel with standard deviation equal to 10 pixels. Since the underlying line integrals are smoothly varying (forward projection is a smoothing operation), the expression within the Σ_u is approximately zero-mean. Minimizing the sum of squared error therefore discourages the presence of high frequency variations as a result of residual MAD bar patterns. The estimation of a_κ was performed for each projection over 200 pixels behind the object and the final scalar a_κ values was obtained from averaging over all projections to reduce noise.

Following all correction steps, the line integrals are obtained according to the following equation and used as inputs for reconstructions:

$$l = \frac{-log\left(\frac{y/A}{M_b/A}\right)}{a_\kappa\langle\kappa^*\rangle_v + 1 - \overline{a_\kappa\langle\kappa^*\rangle_v}}. \tag{A.7}$$

References

Bartolac S, Graham S, Siewerdsen J and Jaffray D 2011 Fluence field optimization for noise and dose objectives in CT Med. Phys 38 S2 [PubMed: 21978114]

Gang GJ, Siewerdsen JH and Stayman JW 2017 Task-driven optimization of fluence field and regularization for model-based iterative reconstruction in computed tomography IEEE Trans. Med. Imaging 36 2424–35 [PubMed: 29035215]

Gang GJ, Stayman JW, Zbijewski W and Siewerdsen JH 2014 Task-based detectability in ct image reconstruction by filtered backprojection and penalized likelihood estimation Med. Phys 41 081902 [PubMed: 25086533]

Gomes J, Gang G, Mathews A and Stayman J 2017 An investigation of low-dose 3D scout scans for computed tomography Proc. SPIE 10132 101322M

Graham SA, Siewerdsen JH and Jaffray DA 2007 Intensity-modulated fluence patterns for task-specific imaging in cone-beam CT Proc. SPIE 6510 651003

Hansen N and Ostermeier A 1996 Adapting arbitrary normal mutation distributions in evolution strategies: the covariance matrix adaptation Proc. of IEEE Int. Conf. on Evolutionary Computation (IEEE) pp 312–7

Harpen MD. 1999; A simple theorem relating noise and patient dose in computed tomography. Med. Phys. 26:2231. [PubMed: 10587203]

Hermus JR and Szczykutowicz TP 2016 Two-dimensional dynamic fluid bowtie attenuators J. Med. Imaging 3 13502

Heuscher DJ and Noo F 2011 CT dose reduction using dynamic collimation IEEE Nuclear Science Symp. and Medical Imaging Conf. (IEEE) pp 3470–3

Hsieh SS and Pelc NJ 2013 The feasibility of a piecewise-linear dynamic bowtie filter Med. Phys 40 031910 [PubMed: 23464325]

Hsieh SS and Pelc NJ 2014 Algorithms for optimizing CT fluence control Proc. SPIE 9033 90330M

Hsieh SS, Fleischmann D and Pelc NJ 2014 Dose reduction using a dynamic, piecewise-linear attenuator Med. Phys 41 021910 [PubMed: 24506631]

Joseph PM and Spital RD 1978 A method for correcting bone induced artifacts in computed tomography scanners J. Comput. Assist. Tomogr 2 100–8 [PubMed: 670461]

Kalra MK, Maher MM, Toth TL, Hamberg LM, Blake MA, Shepard JA and Saini S 2004 Strategies for CT radiation dose optimization Radiology 230 619–28 [PubMed: 14739312]

Liu F, Yang Q, Cong W and Wang G 2014 Dynamic bowtie filter for cone-beam/multi-slice CT PLoS One 9 e103054 [PubMed: 25051067]

Mao A, Shyr W, Gang GJ and Stayman JW 2018 Dynamic beam filtering for miscentered patients Proc. SPIE 10573 105730U

Mathews A, Gang G, Levinson R, Zbijewski W, Kawamoto S, Siewerdsen J and Stayman J 2017 Experimental evaluation of dual multiple aperture devices for fluence field modulated x-ray computed tomography Proc. SPIE 10132 1013220

Mathews AJ, Steven Tilley I I, Gang G, Kawamoto S, Zbijewski W, Siewerdsen JH, Levinson R and Stayman JW 2016 Design of dual multiple aperture devices for dynamical fluence field modulated CT Conf. Proc. Int. Conf. on Image Formation in X-Ray Computed Tomography vol 2016 (NIH Public Access) p 29

Shunhavanich P, Hsieh SS and Pelc NJ 2015 Fluid-filled dynamic bowtie filter: a feasibility study Proc. SPIE 9412 94121L

Stayman JW, Mathews A, Zbijweski W, Gang GJ, Siewerdsen JH, Kawamoto S, Blevis I and Levinson R 2016 Fluence-field modulated x-ray CT using multiple aperture devices Proc. SPIE 9783 97830X

Szczykutowicz TP and Hermus J 2015 Fluid dynamic bowtie attenuators Proc. SPIE 9412 94120X

Szczykutowicz TP and Mistretta CA 2013a Design of a digital beam attenuation system for computed tomography: part I. System design and simulation framework Med. Phys 40 021905 [PubMed: 23387753]

Szczykutowicz TP and Mistretta CA 2013b Design of a digital beam attenuation system for computed tomography. Part II. Performance study and initial results Med. Phys 40 021906 [PubMed: 23387754]

Szczykutowicz TP and Mistretta CA 2014 Experimental realization of fluence field modulated CT using digital beam attenuation Phys. Med. Biol 59 1305–26 [PubMed: 24556823]

Toth T, Ge Z and Daly MP 2007 The influence of patient centering on CT dose and image noise Med. Phys 34 3093–101 [PubMed: 17822016]

Toth TL 2002 Dose reduction opportunities for CT scanners Pediatric Radiol. 32 261–7

Toth TL, Tkaczyk EJ and Hsieh J 2006 Method and apparatus of radiographic imaging with an energy beam tailored for a subject to be scanned US Patent Specification 7,076,029

Wang W, Gang GJ, Mao A, Sisniega A, Siewerdsen JH and Stayman JW 2018 Volume-of-interest CT imaging with dynamic beam filtering using multiple aperture devices Proc. of the Int. Conf. on Image Formation in X-ray Computed Tomography pp 213–7

Yin Z, Yao Y, Montillo A, Wu M, Edic PM, Kalra M and De Man B 2015 Acquisition, preprocessing, and reconstruction of ultralow dose volumetric ct scout for organ-based ct scan planning Med. Phys 42 2730–9 [PubMed: 25979071]

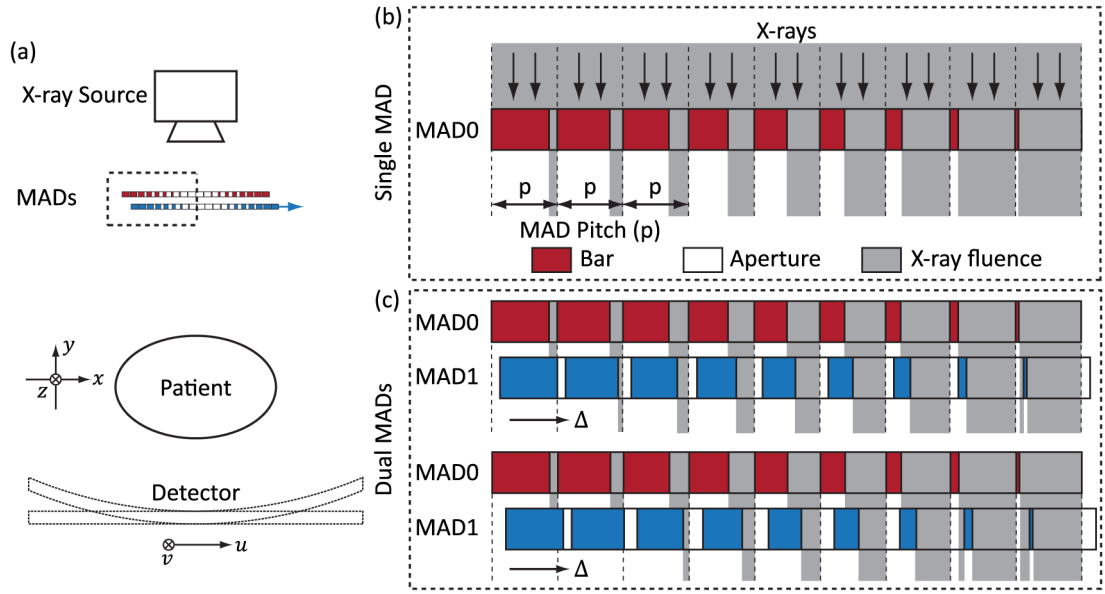

Figure 1.

Multiple aperture devices (MADs) as a pre-patient beam filter. A single MAD consists of fine-scale bars and apertures of different widths that control the amount of x-ray attenuation within each period. A dual-MAD (designated as MAD0 and MAD1) arrangement introduces additional modulation patterns as a function of MAD1 displacement.

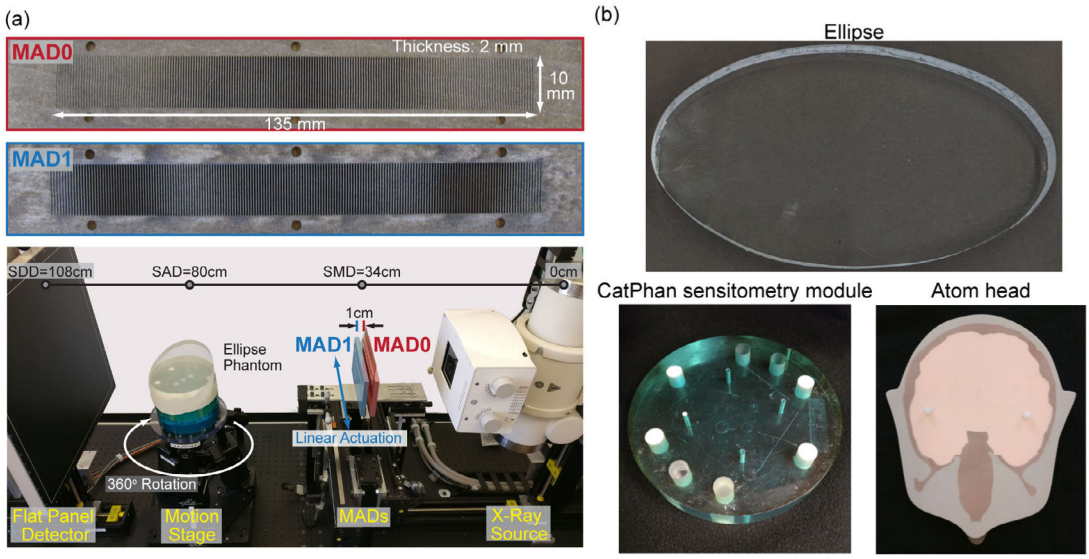

Figure 2.

(a) Dual MAD filter and installation on an experimental imaging bench. (b) Ellipse, CatPhan sensitometry module, and Atom head phantom used for FFM acquisition and image quality assessment.

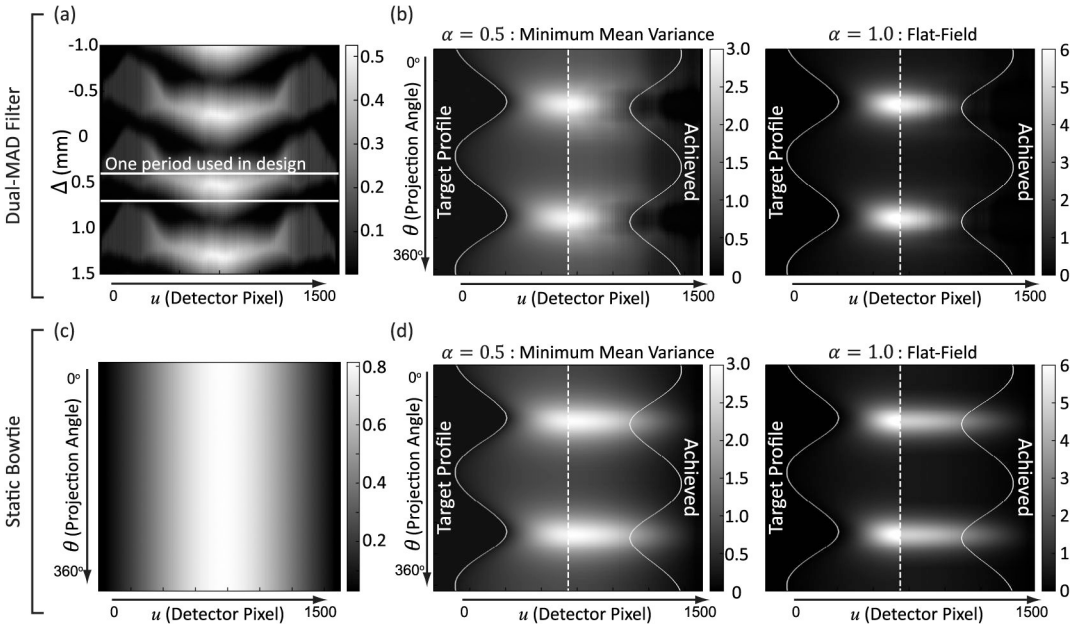

Figure 3.

(a) Modulation profiles measured from the CBCT bench as a function of MAD1 displacements, Δ. (b) The FFM profiles designed for the elliptical phantom corresponding to the α = 0.5 and α = 1.0 objectives. Target profiles calculated from equation (1) (left) shows good agreement with those achieved by the dual-MAD filter on the bench (right). (c) Modulation profiles provided by the bowtie as measured from the CBCT bench as a function of projeciton angles. (d) Target FFM profiles (left) compared with achieved profiles by the bowtie (right), showing poorer agreement compared to the dual-MAD, espeically for narrow profiles.

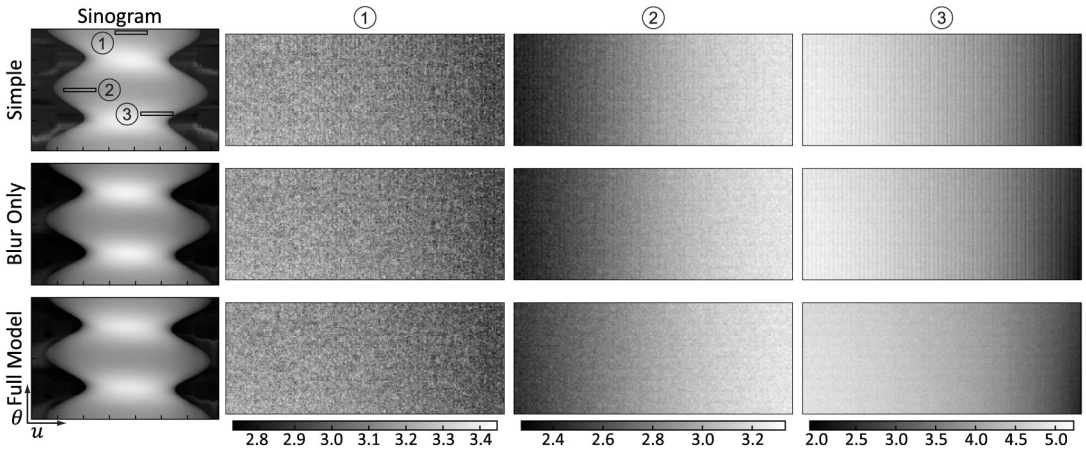

Figure 4.

Corrected line integral data following the simple, blur only, and full model correction algorithms. The sinogram is displayed on the left, with three zoomed ROIs on the right. Bar patterns are obvious following the simple and blur only correction methods, and are mostly removed in the full model corrected data.

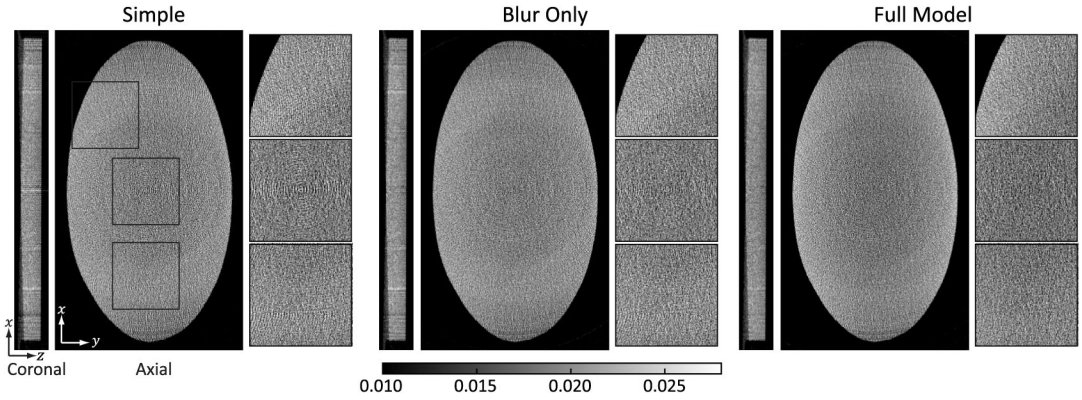

Figure 5.

Reconstructions of the ellipse phantom following the simple, blur only, and full model corrections. A coronal slice, an axial slice, and three axial ROI are presented. Consistent with figure 4, reconstruction following the simple correction has severe ring artficats in the axisl slice and vertical bar patterns in the coronal slices. These artifacts are mostly suppressed by the full model correction method.

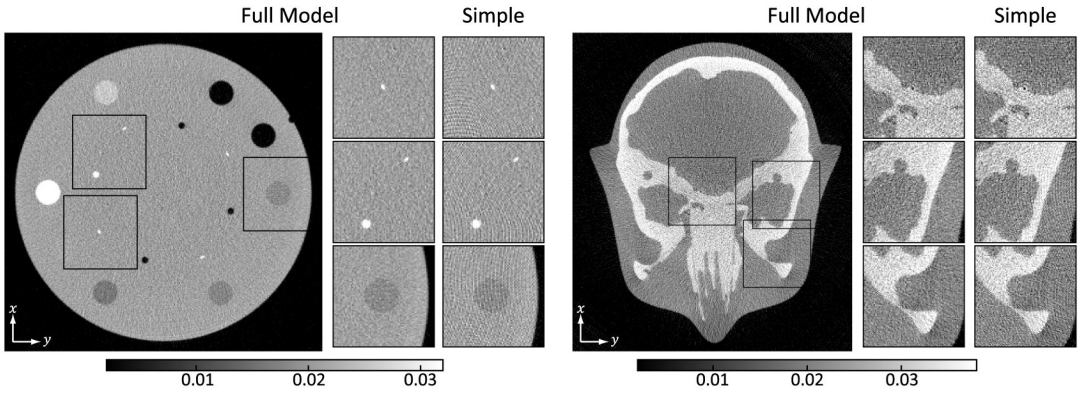

Figure 6.

Reconstructions of the CatPhan sensitometry model and the Atom head phantom. An axial slice through the reconstruction and three ROIs are presented for the full model correction. The same three ROIs are shown for the simple correction method for comparison of the severity of ring artifacts, resolution, and phantom details such as wires, contrast inserts, and bone boundary.

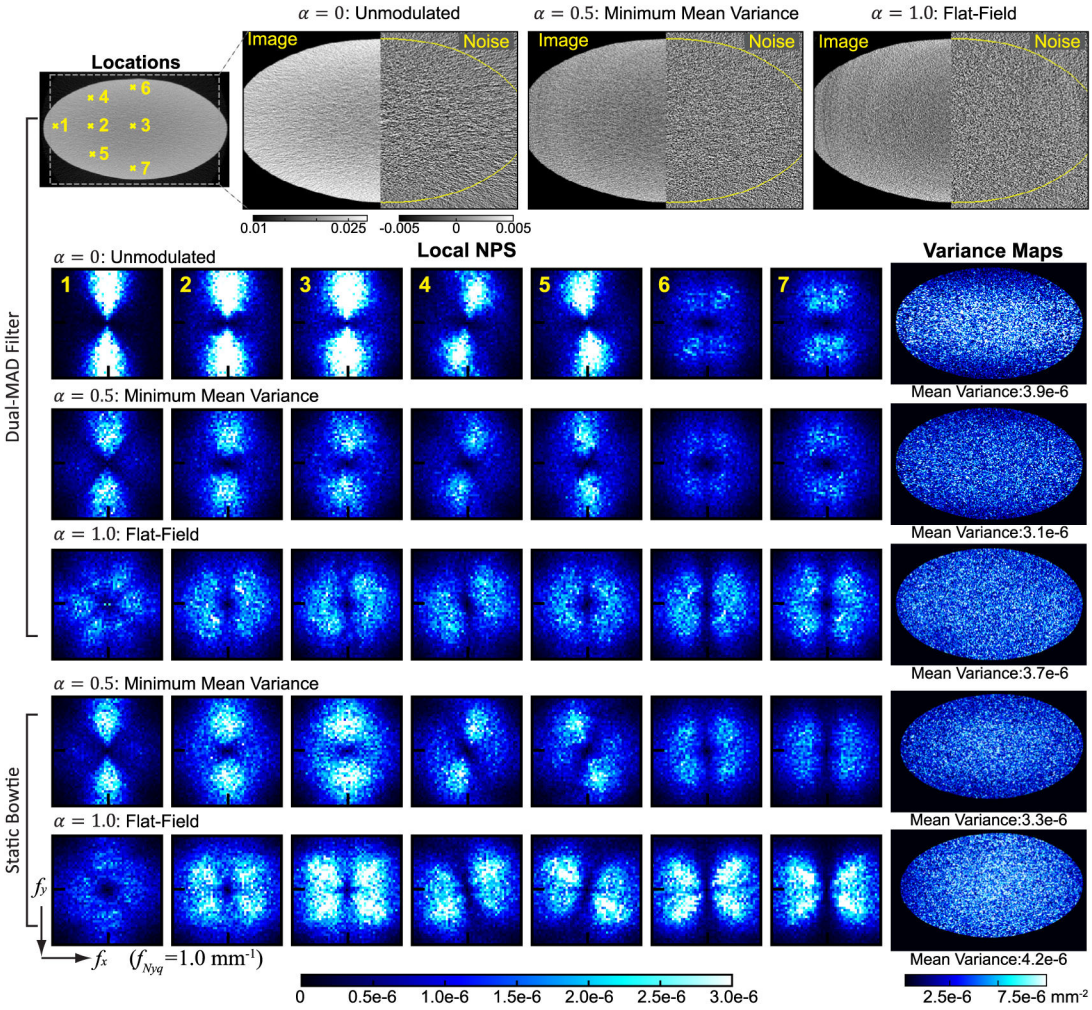

Figure 7.

Noise characteristics as a result of the three MAD-enabled FFM strategies in section 2.3.2: unmodulated ($\alpha = 0$), minimum mean variance ($\alpha = 0.5$), and flat-field ($\alpha = 1.0$). Top: reconstructed slices and difference images between two repeated scans showing directionally correlated noise in the $\alpha = 0$ case and more isotropic noise in the $\alpha = 1.0$ case. Bottom: local NPS and variance maps further illustrating directionality of noise correlation and noise magnitude. Noise characteristics from bowtie acquisitions are also presented for comparison.

Table 1.

System geometry of the experimental CBCT benchtop system, as well as variables and notation for the data forward model and MAD corrections.

Notation	Definition/Description	Dependence
CBCT system parameters		Values
SAD	Source-to-axis distance	800 mm
SDD	Source-to-detector distance	1040 mm
SMD	Source-to-MAD distance	340 mm
—	Distance between two MADs	1 cm
Data forward model		
θ	Projection angle	0°–360°
y	Measured, offset corrected data	u, v, θ
l	Line integrals	u, v, θ
t	Pulse width	θ
Δ_θ	MAD1 displacement as a function of θ	θ
g_{B_0}	Gain associated with beam shape and bare-beam fluence	u, v
g_D	Gain associated with detector sensitivity	u, v
g_M	Gain associated with MADs	u, v, θ
κ	Spectral effect due to MADs	u, v, θ
Calibration scans		
A	Gain scan in air without MADs	u, v, θ
M	Gain scan in air with MADs	u, v, θ
P	Gain scan with PMMA blocks and MADs	u, v, θ